NJC

ROYAL SOCIETY OF CHEMISTRY

PAPER

View Article Online
View Journal | View Issue

Cite this: *New J. Chem.*, 2025, 49, 5716

Nanostructure retention to 1100 °C in soft-templated niobium tungstates using dual-carbon strategy†

Sean C. Wechsler,[a] Alexander Gregg,[a] Coby S. Collins,[a] Santosh Kiran Balijepalli [b] and Morgan Stefik *[a]

Mesoporous metal oxides (MMOs) have diverse applications including energy storage, catalysis, and separation membranes. Block polymer structure directing agents enable the control of morphology and pore size, however preservation of the nanostructure is often limited to a narrow range of heat treatment temperatures which constrains the tailoring of defect chemistries. High temperature treatments typically lead to collapse of the porous structure as surface area is reduced during crystal growth. Here, using a mesoporous niobium tungstate it is shown that neither *in situ* carbon generation nor *ex situ* carbon infiltration alone enable preservation of the ordered mesostructure at temperatures high enough to effectively modify defect chemistry (1100 °C). In contrast, it is shown that a combination of these methods enables preservation of the ordered structure as evidenced by SAXS analysis and electron microscopy. X-ray photoelectron spectroscopy confirmed reduced metal states in the resulting mesoporous materials. This work extends the thermal stability of soft templated niobium tungstates by 500 °C as compared to conventional annealing to enable improved structure preservation after high temperature heat treatment.

Received 17th January 2025,
Accepted 3rd March 2025

DOI: 10.1039/d5nj00229j

rsc.li/njc

Introduction

Mesoporous metal oxides (MMOs) have many modern applications, such as use in gas adsorption/separation,[1–3] catalysis,[4–7] and, energy storage materials.[8–20] MMOs may be fabricated *via* sol–gel synthesis using either 'hard' templates (carbon, silicon)[4,6,16,21–23] or 'soft' templates (micelles, surfactants, polystyrene spheres).[1,3,8,9,11,14,19–21,24–39] The use of hard templates involves the self-assembly of metal precursors around a template of predetermined size and morphology followed by thermal treatments and finally selective etching of the template material. Hard templating methods impart high thermal stability (1000–3000 °C) in the MMO and result in well-ordered mesostructure but have the drawback low tunability of corresponding material dimensions, and typically bring the necessity of etchants such as HF or NaOH which are dangerous and produce significant chemical waste (excluding carbon templates, which may be removed as CO_2 *via* oxidative heating conditions).[4,6,16,22,23]

Conversely, the fabrication of MMOs *via* soft templates permits a high degree of tunability of corresponding material morphology through facile variations in solvent processing.[24,40–47] A challenge with MMOs prepared *via* soft templates is that high-temperature thermal treatments can remove the soft template, leading to unrestricted structural coarsening or collapse of the ordered mesostructure. Such heat treatments nucleate and grow crystals as the oxide densifies and restructures to reduce total surface area.[48–50] When these crystallites become larger than the mesostructured dimensions, the ordered pore/wall structure collapses, first leading to wormlike morphologies and eventually leading to large crystals on the micron length scale.[51–53] The ability to maintain a nanostructure during high temperature treatments is desirable as many metal oxides may not be reduced (form oxygen vacancies) until high temperatures, often >800 °C or during lengthy heat treatments both of which are detrimental towards nanostructure retention.[54–58] Such reduced metal oxides are desirable for applications requiring improved electron transport properties and modified bandgaps.[57–64] Additionally, some crystal phases only form at high-temperature.[65–68] For example, Wadsley–Roth crystal structures often require high temperature crystallization where such niobium tungstates have exhibited good electronic conductivity combined with rapid lithium ion transport.[69–79] In this context, access to MMOs with short diffusion lengths

[a] *University of South Carolina, Department of Chemistry and Biochemistry, Columbia, SC, USA. E-mail: morgan@stefikgroup.com*
[b] *University of South Carolina, Office of the Vice President for Research, Columbia, SC, USA*

† Electronic supplementary information (ESI) available. See DOI: https://doi.org/10.1039/d5nj00229j

significantly enhance device performance.[80,81] Some MMOs are inherently more thermally stable than others due to low metal self-diffusion rates that slow crystal growth such as Al_2O_3,[24,82] SiO_2,[27,83] silicon carbonitrides,[84] and some rare earth MOs which withstand heat treatments up to 700–1500 °C.[28,31,32,85,86] Typically, MMOs such as, TiO_2,[9,30,33,34,51] Nb_2O_5,[8] SnO_2,[87–89] $MgMoO_4$,[15] ZrO_2,[37,88,90] WO_3,[3,36] $TiNbO_x$,[52] and high-entropy alloys consisting of mixtures of aforementioned metals are stable up to 500–700 °C.[19]

Historically, diverse strategies have improved the thermal stability of MMOs fabricated *via* soft templating methods. Additional components have been added to MO precursors such as carbon precursors or oxyphosphides to inhibit the crystallization/mobility of the MO during heat treatments *via* the formation of amorphous glasses that act as a hard template.[10,11,89,91,92] These methods typically led to MMOs with the parent nanostructure stable to temperatures as high as 800 °C in some cases. Later, hard templates were produced *in situ* by carbonizing the soft templates *via* heat treatments in an inert atmosphere to line the walls of the porous material, termed the 'combined assembly by soft and hard' (CASH) method.[93] The carbon produced *via* the CASH method provides a structural barrier to mesopore collapse and allows for TiO_2, Nb_2O_5, and WO_3 to be heated to temperatures of up to 700–800 °C while retaining a high degree of structural ordering.[3,8,29,30,93] Similarly, vapor phase carbon precursors can coat mesopores materials for improved thermal stability.[52,53] While improvements have been made to the thermal stability of soft templated MMOs, their thermal stability remains limited which constrains subsequent processing.

Herein, we describe a block polymer-templated, sol–gel synthesis of a mesoporous niobium–tungsten oxide that alone is limited to ~600 °C heat treatments. To enhance thermal stability, we introduce a liquid carbon precursor (phenol–formaldehyde resol) *via* a pore filling method which builds upon the CASH method to expand the temperature stability of nanostructured niobium tungstates by 500 °C, thus allowing for structure retention as high as 1100 °C. Small-angle X-ray scattering (SAXS), scanning electron microscopy (SEM), and Porod surface area analysis are used to confirm ordered mesostructures before and after carbon treatments. Finally, differential scanning calorimetry (DSC) was used to assess the carbonization thermodynamics of this liquid pore filling process as a standalone method *versus* as a supplement to the previously established CASH method. This work further increases the utility of soft-template based sol–gel methods to enhance the thermal stability of ordered mesoporous materials, thus allowing for further defect tailoring.

Results and discussion

Synthesis of mesoporous niobium tungsten oxides

Scheme 1 shows the fabrication of mesoporous niobium tungsten oxide (Nb–W–O) with block polymer micelles as templates. Poly(ethylene oxide-*b*-butyl acrylate) (PEO-*b*-PBuAc) was prepared

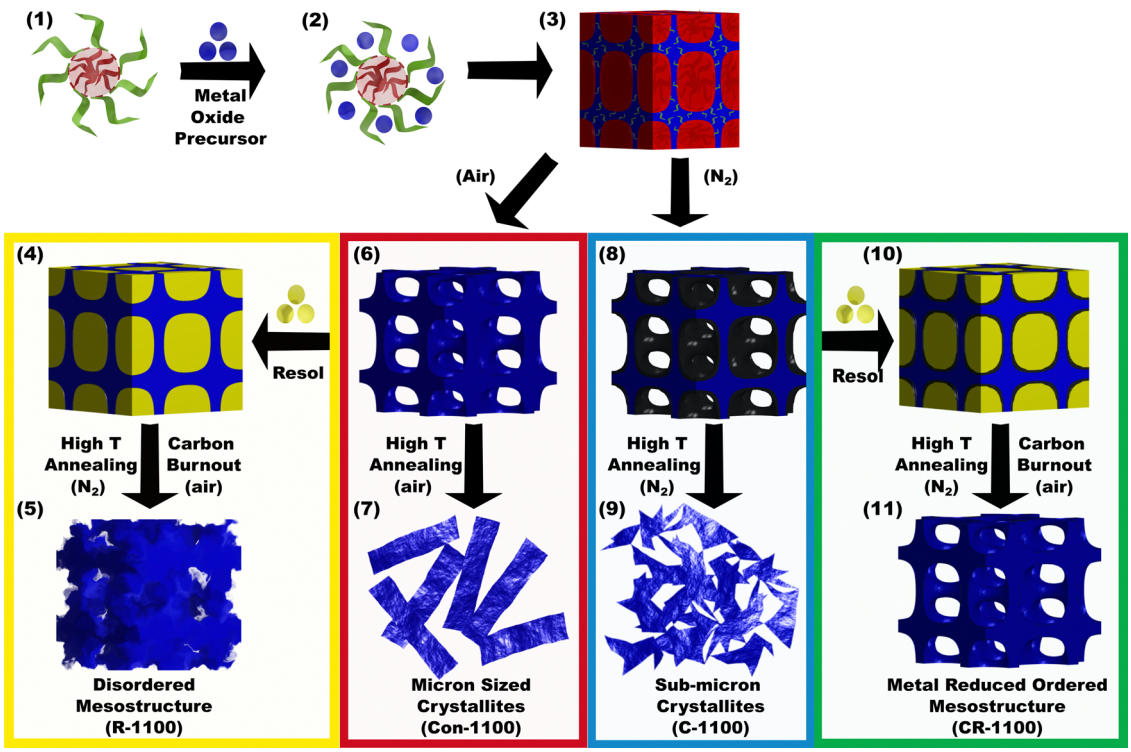

Scheme 1 (1) Polymer micelles are used as templates for (2) metal oxide precursors (blue circles) where evaporative self-assembly leads to (3) a uniform architecture of micelles within an amorphous metal oxide network. (4)–(11) A range of processes were examined for structure preservation during high temperature treatments.

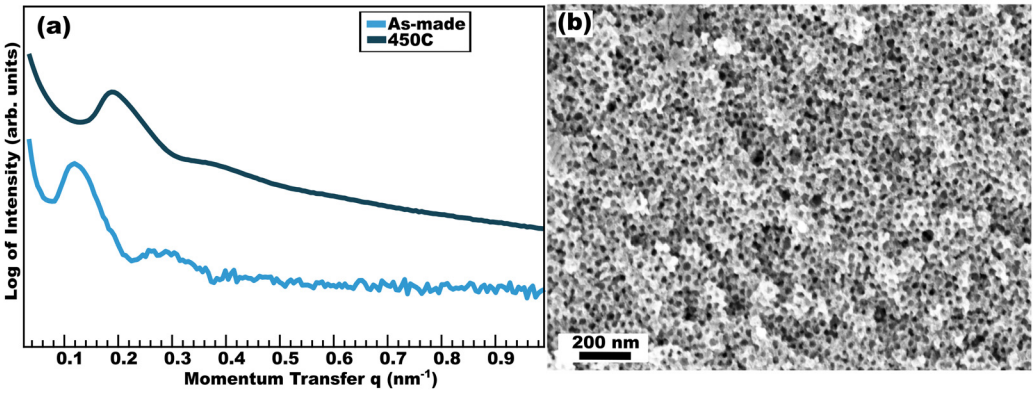

Fig. 1 (a) SAXS and (b) SEM data for low temperature treated samples before high-temperature treatments. The as-made sample was aged at 100 °C before a 450 °C CASH treatment.

as described in the Experimental section (Fig. SI.1 and SI.2, ESI†) for the preparation of micelle templates. The niobium tungsten oxide materials were prepared *via* a variation of established methods[94] using a combination of chloride and alkoxide precursors, involving the partial alcoholysis of tungsten(VI) chloride (WCl_6) in EtOH to form a mixed chloride/alkoxide precursors which was mixed with niobium(V) ethoxide ($NbOEt_5$) and micelle templates under inert atmosphere before casting the solution to a powder.[95,96] The powders were aged to promote crosslinking of the amorphous materials, and then subjected to a range of different heat treatments described in the next section. For each process, a low temperature (450 °C) treatment preceded a subsequent high temperature (1100 °C) treatment. The results of a representative low temperature treatment are presented first before comparing the high temperature results. Fig. 1(a) shows the SAXS pattern for aged sample (as-made) and 450 °C CASH (450C) samples which exhibited principal peaks at q = 0.12 and 0.19 nm^{-1}, respectively, corresponding to d-spacings ($2\pi\ q^{-1}$) of 52.4 and 33.1 nm. This trend indicates the typical shrinkage upon heat treatment as the material densifies. These SAXS patterns are consistent with the structure factor for randomly packed spheres[97,98] where the d-spacing corresponds to the micelle-to-micelle spacing of 32.7 ± 0.3 nm seen in SEM (Fig. 1(b)). A related control sample was prepared at 450 °C under oxidative conditions (without carbon support) which was similar and is described later. The subsequent high temperature studies examined both oxidative and carbonizing conditions and included multiple combinations of different carbon sources (Scheme 1).

Comparison of high temperature treatments

A range of high temperature 1100 °C treatments were examined with the aim of preserving the templated nanostructure. The first case presented follows conventional oxidative processing (Con-1100) which does not include the formation of carbon scaffolds (Scheme 1-(6), (7)). SEM images of the resulting Con-1100 sample indicate the formation of large, 1.63 ± 0.06 micron-sized crystals where coarsening significantly lowered the surface area and removed all trace of the templated mesostructure (Fig. 2(a)). It was observed *via* SAXS that peaks corresponding to a structure factor disappear between 600–700 °C with conventional carbon-free processing (SI.3, ESI†). The CASH method (C-1100) was next examined where calcination in inert atmosphere converts the polymer into a carbon coating that inhibits crystal growth. It was observed *via* SAXS that traces of peaks corresponding to a structure factor were visible at 800 °C, showing an improved temperature stability with the CASH method (SI.3, ESI†). The C-1100 sample, however, exhibited smaller 0.29 ± 0.01 μm crystallites by SEM as compared to Con-1100, but again the thermal coarsening was sufficient to remove all traces of the templated nanostructure (Fig. 2(b) and Schemes 1-(8), (9)). It is likely that the PEO-*b*-PBuAc utilized here has lower carbon yield than other more sp^2-rich polymers which

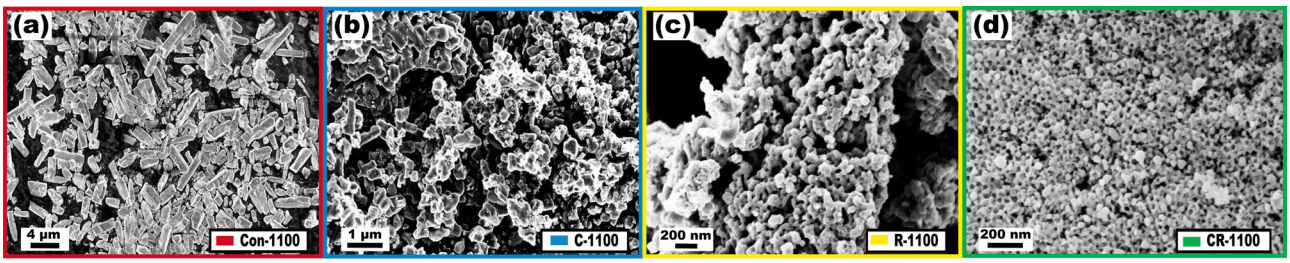

Fig. 2 SEM of samples annealed at 1100 °C (a) with conventional oxidizing conditions (Con-1100), or under nitrogen (b) with *in situ* carbon from the CASH method (C-1100), (c) with resol backfilling (R-1100), or (d) both CASH and resol back filling (CR-1100).

results here in a lower total carbon yield and thus, lesser retention of the nanostructure.[93]

With an aim to preserve the templated mesostructure, a porous oxide sample (450 °C) was prepared in oxidizing conditions and subsequently backfilled with a carbon precursor (R-1100). Specifically, a low molecular weight (<500 g mol^{-1}) phenol–formaldehyde resol was used as the carbon precursor. Resol is a common carbon source used in the soft template literature with well-established carbonization heat treatments.[99–103] The resol was solution deposited into the ordered porous materials after grinding and with *via* rapid stirring for 24 h to promote infiltration into the mesopores.[104,105] The sample was calcined to 1100 °C under nitrogen to carbonize the resol. The SEM images of the resulting R-1100 sample revealed the preservation of 62 ± 2 nm disordered features with limited resemblance to the parent nanostructure (Fig. 2(c) and Schemes 1-(4), (5)). Notably, this increase in the amount of carbon scaffolding led to an enhanced extent of structure preservation that inhibited crystal growth. A combined method using both CASH and resol backfilling was examined in the pursuit of further preserving the parent structure to such high temperatures (CR-1100). The corresponding SEM images revealed that CR-1100 exhibited a high degree of structural ordering, reminiscent of the parent templated MMOs. Both 18.3 ± 0.3 nm crystallites and 28.5 ± 0.5 nm pores were apparent in CR-1100 (Fig. 2(d) and Schemes 1-(10), (11)).

This collection of samples was next examined with SAXS as an ensemble method to check for nanoscale features over a larger region and estimate the specific surface area. The carbon, if present, was burned out of the samples before SAXS such that all samples were purely oxide (carbon-free, *vida infra*). These data are presented using absolute intensity on Porod plots where the constant $I \times q^4$ values at high-q are proportional to the mass-specific surface area (Fig. 3(a)).[106] Similar to the parent nanostructure with a principle SAXS peak at q = 0.12 nm^{-1}, a broad peak was visible for R-1100 and CR-1100 at q = 0.13 nm^{-1} which is most apparent in Fig. 3(b) and corresponds to a d-spacing of 48 nm. In contrast, C-1100 and Con-1100 did not have apparent peaks in the measurable q-range, consistent with the substantial coarsening that was observed *via* SEM. With absolute scattering intensities, the Porod region allows the comparison of sample surface areas (described in experimental). Here, CR-1100 had specific surface area of 24.2 m^2 g^{-1} whereas R-1100 had 12.5 m^2 g^{-1} and C-1100/Con-1100 each had less than 2 m^2 g^{-1}, consistent with the coarsening and loss of the templated nanostructure apparent in SEM images (Table 1). The thermal stability of the CR-1100 nanostructure after carbon removal was examined by SAXS by further heating the sample to 600 °C and 700 °C in air (SI.4, ESI†). The structure factor peak apparent at q = 0.13 nm^{-1} in the 600 °C sample was absent in the sample heated to 700 °C, suggesting loss of nanostructure control. Thus the thermal stability of the CR-1100 nanostructure after carbon removal is similar to that of conventionally templated oxide without carbon scaffolds (SI.3, ESI†). Thus, the combination of SEM and SAXS data demonstrated that the combination of CASH and resol backfilling led to substantially improved nanostructure preservation up to 1100 °C.

Table 1 Surface area values determined from analysis of the Porod data presented in Fig. 3

Sample name	Surface area (m^2 g^{-1})	Error in surface area (m^2 g^{-1})
Conventional (Con-1100)	0.14	0.01
CASH-1100 (C-1100)	1.83	0.05
Resol backfill (R-1100)	12.5	0.2
CASH and resol backfill (CR-1100)	24.2	0.6

Properties of CR-1100 sample

The oxidation states and crystal structure were further characterized for CR-1100 after removing the residual carbon oxidatively at 450 °C. As elaborated in the introduction, high temperature heat treatments under inert atmosphere are often used to induce defect states which may improve the material properties, thus the oxidation states were measured using XPS. Fig. 4(a) shows the Nb 3d spectra for CR-1100, which shows a mixture of Nb^{4+} and Nb^{5+} oxidation states at 206.1 eV and 207.8 eV respectively. The same trend is demonstrated for the W 4f spectra (Fig. 4(b)), where a mixture of W^{5+} and W^{6+} oxidation states is apparent at 35.3 eV and 36.9 eV. The O 1s

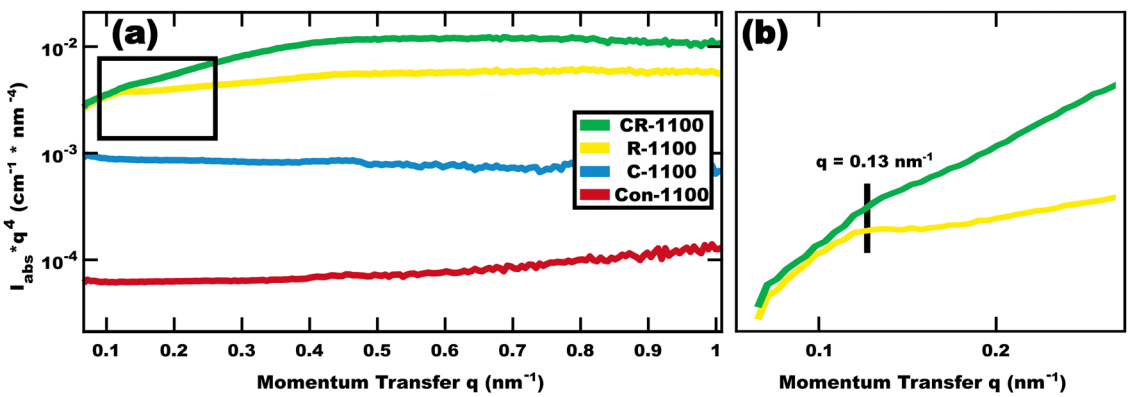

Fig. 3 (a) Absolute intensity SAXS data presented as Porod plots for all-oxide samples with carbon burned out, if present. The intensity as plotted (Porod region) is proportional to the specific surface area. (b) Zoom-in of the SAXS features in R-1100 and CR-1100.

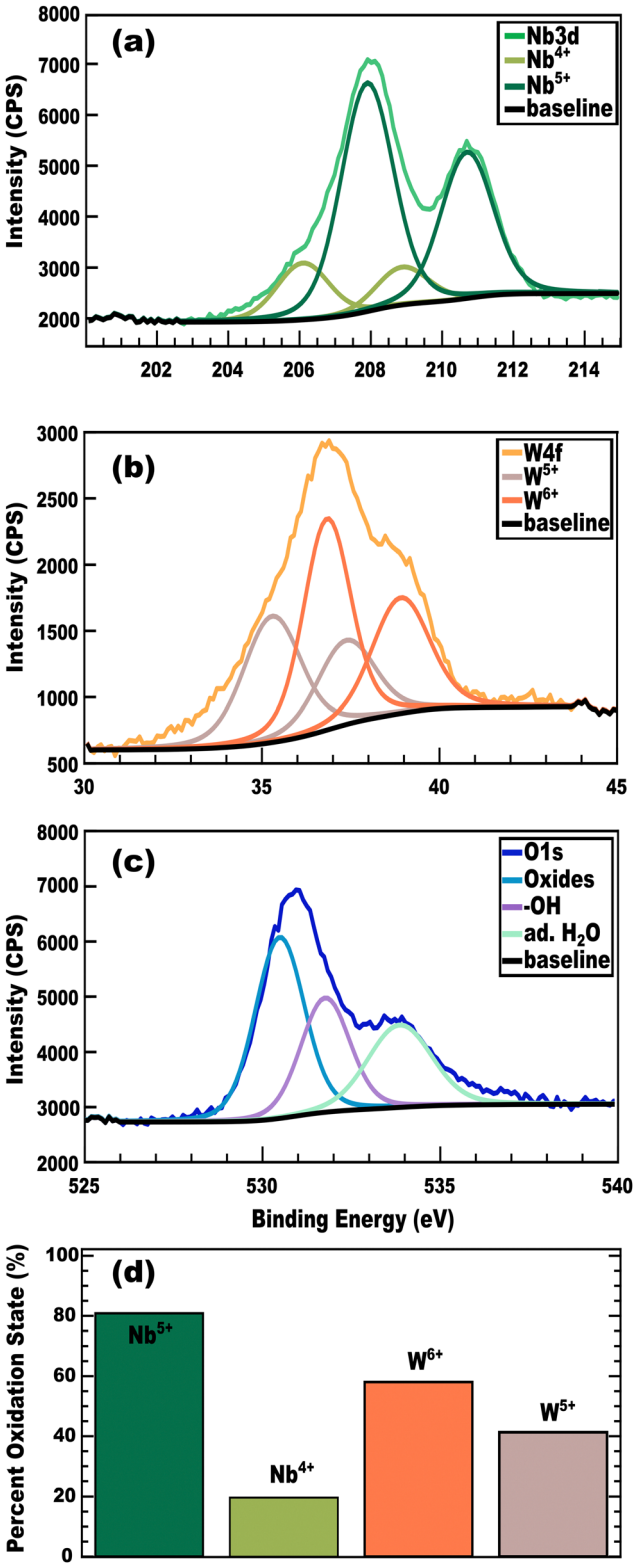

Fig. 4 XPS of mesoporous CR-1100 after carbon removal showing partial metal reduction: (a) Nb 3d, (b) W 4f, (c) O 1s spectra, and (d) summary plot.

spectra in Fig. 4(c) includes contributions from lattice oxygen (530.5 eV), surface hydroxyl groups (531.8 eV), and adsorbed H_2O (533.9 eV), the latter two of which are often erroneously reported as oxygen vacancies.[107] These trends are summarized for CR-1100 in Fig. 4(d) where 19.95% of the Nb and 42.09% of the W are reduced (Nb^{4+}/W^{5+}). In contrast, sample Con-1100 did not exhibit reduced metal states by XPS (SI.5, ESI†). Oxygen vacancies can form as a result of oxygen loss to either (1) evaporation of lattice oxygen when annealed with low oxygen partial pressure and/or (2) carbothermal reduction of metal oxides to release CO_2.[108,109] XPS survey scans for both CR-1100 (before and after carbon burnout) and Con-1100 are presented in SI.6 (ESI†). The carbon peak intensity (285 eV) of CR-1100 decreases markedly after the carbon burnout such that the trace surface carbon is commensurate to that resulting from conventional heating to 1100 °C in air (Con-1100). This carbon removal was also evidenced with Raman spectroscopy (Fig. 5) with the complete removal of detectable D, G, and G′ bands.[110]

In terms of crystallization, it is well known that carbon scaffolds inhibit crystal growth due to the formation of amorphous glasses that impede diffusion and reorganization (*vida supra*). Wide-angle X-ray scattering (WAXS) was used to measure diffraction and the WAXS of Con-1100 was consistent with a $Nb_{14}W_3O_{44}$ reference pattern (SI.7, ESI†). In contrast, R-1100 and CR-1100 exhibited broad diffraction peaks indicative of smaller crystallite sizes which were attributed to the additional carbon further inhibiting crystallization. The diffraction peaks were rather equivocal to interpret into specific phases, however, the positions were consistent with orthorhombic Nb_2O_5 and monoclinic WO_3 (SI.8, ESI†). These results highlight the potential for the CR method, combining CASH and resol back filling, to uniquely enable mesostructure preservation through higher temperature heat treatments that enable defect tailoring.

Improved carbonization from CR method

The excellent structure retention of CR-1100 is perhaps surprising when considering that R-1100 was only different by lacking trace carbon from the CASH process. It was previously reported that the polycondensation reaction that occurs as the resol converts to carbon during heat treatment can be catalytically activated through local interactions.[102] To check for such synergistic interactions, DSC was employed to compare the

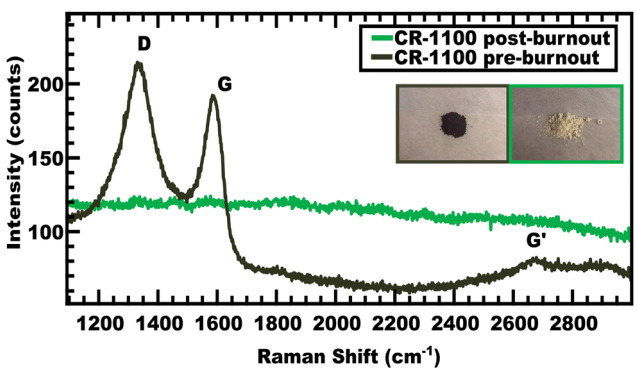

Fig. 5 Raman spectra of CR-1100 before carbon burnout (inset image of black powder) and after carbon burnout (inset image of white/yellow powder).

polycondensation events that occurred in the production of Con-1100 and CR-1100. TGA of the plain PF resol (SI.9, ESI†) was first examined to distinguish between initial solvent evaporation (IPA, <120 °C) and later condensation events. The thermodynamics of carbonization were compared using established methods with model-free kinetics where the curing of the resol can be treated as a single step, 1st order reaction where the peak point (T_p) of the DSC condensation event at each heating rate (β, 2–20 °C min^{-1}, SI.10, ESI†) is correlated with the activation energy (E_a).[101–103,111–115] Arrhenius-like plots were generated per the Kissinger method[116] to derive a plot of $\ln(\beta/T_p^2)$ *vs.* $1000/T_p$ with a slope of E_a/R, where R is the gas constant (Fig. 6(a)). Here resol polymerization conditions were varied: starting from pure resol (''resol only''), starting from conventional MMO (450 °C heated in air) that was backfilled with resol (''R-1100''), and starting from CASH-based MMO (450 °C under nitrogen) that was backfilled with resol (''CR-1100''). Thus, these measurements allow the comparison of resol polymerization conditions. This analysis identified the activation energy of condensation to be 54.8 kJ mol^{-1} for PF resol-only whereas the combination of CASH and resol (CR-1100) had an activation energy of 22.8 kJ mol^{-1} (Fig. 6(b)). This reduced activation energy shows that the CASH carbon can act as a catalyst to enhance the polymerization of resol. For comparison, the activation energy for resol condensation within porous oxide (R-1100) was 87.5 kJ mol^{-1}, showing that the bare oxide surface inhibits resol condensation relative to a carbon surface. Thus, the results of CR-1100 are explainable by the CASH carbon increasing the carbon yield from resol which enhanced nanostructure preservation through high temperature heat treatments.

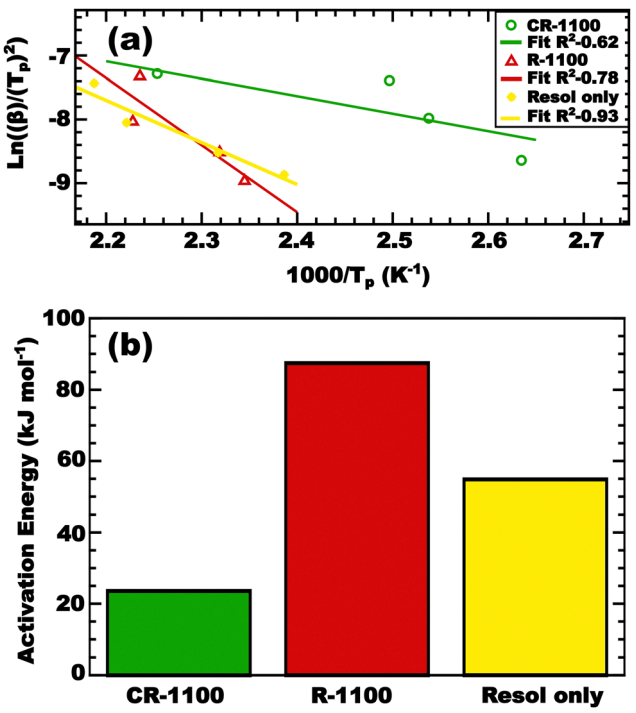

Fig. 6 (a) Kissinger plots derived from peak temperature (T_p) of variable heat rate (β) DSC endotherms of CR-1100 (green circles), R-1100 (red triangles), and resol only (yellow stars). (b) The linear best fits were used to determine the activation energies for resol polymerization in different local environments.

Conclusion

A soft templating strategy to enhance nanostructure integrity through high temperature heat treatments was advanced. Neither the *in situ* carbon from the CASH method nor resol back filling alone enabled nanostructure retention for the investigated Nb–W–O samples up to 1100 °C. Rather, the CR method, combining CASH with resol backfilling (CR-1100), enabled the best retention of the micelle templated nanostructures up to 1100 °C, thus adding several hundred degrees to the stability window for the investigated materials. This mesostructure retention was confirmed using both SEM and SAXS analysis. The properties of the resulting high temperature treated materials were examined using XPS and WAXS where reduced metal oxidation states were enabled along with an inhibition of crystallization with increasing carbon quantity during the 1100 °C treatment. The resol polymerization thermodynamics were investigated, where the CR method lowers the polycondensation activation energy by 74% relative to resol backfilling into oxide alone (R-1100). This approach demonstrates a convenient strategy to preserve the nanostructure derived from soft templated materials for the realization of mesoporous metal oxides with properties uniquely accessible with high temperature heat treatments.

Experimental

Materials

Ethanol (EtOH 200 proof, 100%, Fisher) was dried over activated molecular sieves (3 Å, 8–12 mesh, Acros Organics) for several days before use. Poly(ethylene oxide) methyl ether (H_3C-PEO-OH), M_n = 20 000 g mol^{-1} (20k PEO-OMe, Aldrich), butyl acrylate monomer (99% stabilized, Acros Organics) was first passed over a column of basic alumina (40–300 μm, Acros Organics), to remove the inhibitor, 2-bromopropionic acid (>99%, Aldrich), *N*,*N*,*N*′,*N*″,*N*′-pentamethyldiethylenetriamine (PMDETA, Beantown), *N*,*N*′-dicyclohexylcarbodiimide (DCC, Aldrich), 4-(dimethylamino)-pyridine (DMAP, 99%, Aldrich), dichloromethane (DCM, ACS certified, Fisher), copper(II)bromide (99%, Acros Organics), ascorbic acid (VWR), dimethyl formamide (DMF, ACS grade, Fisher), anisole (99%, Beantown), tetrahydrofuran (THF, unstabilized, 99.8%, Thermo), phenol (ACS grade, VWR), deionized water (H_2O, Wards), sodium hydroxide pellets (NaOH, ACS grade, Macron Fine Chem.), formaldehyde (37% in methanol, Thermo), hydrochloric acid (37%, trace metal grade, Fisher), isopropyl alcohol (100%, Labchem), deuterated chloroform (99.8%, Cambridge Isotope Labs), niobium(V) ethoxide ($Nb(OEt)_5$ 99.9%, Fisher) and tungsten(VI) chloride (WCl_6, 99.9%, Aldrich) were stored in an argon glovebox prior to use temperature grade Kapton tape (Mcmaster), DSC boats (Aluminum, DSC consumables),

Polymer synthesis and characterization

Poly(ethylene oxide-*b*-butyl acrylate) (PEO-*b*-PBuAc) block polymer was synthesized by a two-step method. First, a PEO macroinitiator was synthesized using a Steglich esterification[97] followed by activators regenerated by reversible-deactivation radical polymerization (RDRP).[117] The conditions for the DCC/DMAP Steglich esterification between 2-bromopropionic acid and (20k) PEO-Me are listed in detail elsewhere.[97] The following conditions were used for the RDRP with PEO-Br : PMDETA : Cu(II)Br : ascorbic acid : butyl acrylate of 1 : 1 : 1 : 0.45 : 1000. Inhibitor-free butyl acrylate (14.401 mL, 99.9 mmol) was added to 20 000 g mol^{-1} PEO-Br macroinitiator (2.04 g, 0.101 mmol) of in a 100 mL round-bottom flask along with of anisole (1.44 mL), Cu(II)Br (24.4 mg, 0.109 mmol), and ascorbic acid (7.9mg, 0.449 mmol). Separately, a syringe of DMF and with dissolved PMDETA (20.88 μL, 0.10 mmol) was prepared. Then, the solution flask was sealed with a rubber septa and copper wire and then nitrogen sparged for 30 min before the DMF/PMDETA solution was added to solubilize the Cu(II)Br. The flask was added to a 70 °C oil bath while stirring for 24 h, at which point the reaction mixture became sufficiently viscous. The reaction vessel was placed in the freezer for an hour to cool and then the polymer was dissolved in DCM so the mixture could be passed over a basic alumina column to remove the remaining copper catalyst. The polymer/DCM mixture was dialyzed in dichloromethane for 72 h. The molar mass of the PBuAc block (110 000 g mol^{-1}) was characterized by comparison to the known PEO (M_n = 20 000 g mol^{-1}) using a Bruker Avance III HD 300 ^{1}H NMR and then the molar mass dispersity ($Đ$) was measured using gel permeation chromatography (GPC) (Fig. SI.1 and SI.2, ESI†). NMR samples were prepared in deuterated chloroform ($CDCl_3$) at a concentration of 10 mg mL^{-1}. The GPC data was collected Waters 515 HPLC pump, Waters 2410 refractive index detector, three styragel columns (HR2, HR4, and HR5) in the effective molecular weight range of 0.5–20, 5–600, 50–4000 kg mol^{-1}, respectively. The eluent was THF at a temperature of 25 °C and a flow rate of 1 mL min^{-1}. The data was analyzed using custom MATLAB scripts (**https://stefikgroup.com//GPC/**). The instrument was calibrated with polystyrene standards (800, 560, 320, 180, 100, 43, 20, 10, 4.5, 2.1, 1.0, 0.27 kg mol^{-1}) received from Polymer Standards ServiceGPC samples were prepared by dissolving the PEO-*b*-PBuAc in THF with a concentration of 10 mg mL^{-1} and filtered through a 0.2 μm syringe filter prior to injection.

Carbon precursor synthesis and characterization

Phenol–formaldehyde resol synthesis was done following the procedure explained in detail elsewhere.[100] In short, phenol (5.65 g, 60.0 mmol) was dissolved in a NaOH/H_2O (20% wt, 0.24 g, 6 mmol). To this solution, formaldehyde (3.6 g, 120 mmol) was added dropwise and was stirred for 30 m before neutralizing to ~pH 7 with HCl. Then, isopropyl was used to recrystallize out any NaCl *via* heating at 90 °C. The resol was stored at 0 °C before use to prevent further reaction. The same GPC and sample preparation methods were used to measure molar mass dispersity ($Đ$) and molecular weight (SI.11, ESI†) as described above.

Sol–gel synthesis of niobium tungstates

To fabricate Nb–W–O powders, a micelle solution was prepared using PEO-*b*-PBuAc at a concentration of 10 mg mL^{-1} in EtOH. This solution was stirred for at least 3 hours to promote micelle size equilibration before use. Meanwhile, the precursors were prepared by dissolving WCl_6 (0.041 grams, 0.103 mmol) in EtOH to a concentration of 500 mg mL^{-1} in inert conditions. Chlorine gas and hydrochloric acid are generated at this point, so caution is advised. The quantity of precursors corresponds to the molar ratio of tungsten and niobium in $Nb_{14}W_3O_{44}$. This solution was amber when first dissolved but would rapidly change to green then blue if exposed to air as the WCl_6 was first dimerized then hydrolyzed ($W(OHt)_6$).[95,96] Still under inert conditions, the mixed tungsten chloride alkoxide solution was added rapidly to 2.5 mL of micelle solution while stirring, promptly followed by $Nb(OEt)_5$ (0.154 grams, 0.484 mol). This solution rapidly turned amber after the first addition then egg-yolk yellow after both additions. It was found to be important that the WCl_6 solution was used immediately after mixing while still amber for phase purity in the Con-1100. This sol–gel solution was poured into a preheated (100 °C) Teflon dish to evaporate for 24 h. Upon addition to the dish, the solution rapidly turned dark green and then amber after complete drying.

CASH and resol method annealing conditions

The aged sol–gel solution was scraped into ceramic crucibles for annealing under various conditions described visually in Scheme 1. Con-1100 was annealed in a box furnace with atmospheric conditions by ramping from RT-1100 °C@10 °C min^{-1} with a 30 m hold. C-1100 was annealed in a tube furnace with flowing N_2 using previously established CASH heating conditions[93] by ramping from RT-450 °C@1 °C min^{-1} with a 3 h hold at 450 °C before ramping 450 °C to 1100 °C@10 °C min^{-1} with a 30 m hold. R-1100 was fabricated *via* annealing aged powder from RT-450 °C@10 °C min^{-1} in the box furnace (atmospheric conditions) with a 3 h hold. Then the sample was ground *via* pestle and the sample was saturated with a large excess (10 : 1, by mass) of liquid carbon precursor and stirred rapidly for 24 h to infiltrate the resol into the pores of the material. Then, this resol/metal oxide suspension was transferred to a crucible and annealed from RT-450 °C@1 °C min^{-1} under flowing N_2 with a 3 h hold at 450 °C before ramping to 1100 °C@10 °C min^{-1} with a 30 m hold (N_2). CR-1100 was fabricated by following the CASH method annealing conditions (C-1100), then the resol infiltration and heating conditions used for the R-1100. Before characterization, the carbon from both C-1100 and CR-1100 was burned out in atmospheric conditions for 12 h at 450 °C, until the powders were yellow. For structure retention experiments with control samples and post-carbon removal CR-1100 samples, the powders were heated to the corresponding temperature (600 °C, 700 °C, or 800 °C) in a box furnace@10 °C min^{-1} and held at the target temperature for 30 m.

SEM characterization

Oxide powders were imaged on adhesive carbon tape using a Zeiss Ultraplus thermal field emission SEM using an accelerating voltage of 3 keV and an in-lens secondary electron detector. An ideal working distance was found to be 3.0 mm, and all images were acquired between 50 000× and 400 000× magnification (dependent on sample feature size). Structural dimensions were measured in ImageJ using an average of 300 measurements for each value. The presented error corresponds to the standard error of the mean.

X-ray scattering methods

Wide-angle and small-angle X-ray scattering (WAXS/SAXS) measurements were performed at the South Carolina SAXS Collaborative using a SAXSLab Ganesha instrument. A Xenocs GeniX3D microfocus source was used with a Cu target to create a monochromatic beam with a wavelength of 0.154 nm. The instrument was calibrated with a NIST reference material 640d silicon powder, with a reference peak position of 2θ = 28.44°, where 2θ represents the total scattering angle. A Pilatus 300 K detector (Dectris) was used to collect the 2D scattering patterns. The detector exhibited a nominal pixel dimension of 172 × 172 μm^2. WAXS measurements were conducted with a sample-to-detector distance was 112.1 mm with an X-ray flux of ∼36.3 million photons s^{-1} upon the sample. The 2D images were azimuthally integrated to yield the scattering vector intensity. SAXS measurements for Porod surface area analysis were acquired with an X-ray flux of ∼16.1 million photons s^{-1} and a sample–detector distance of 1040 mm. Finely powdered samples were spread onto Kapton tape as a homogeneous and thin layer. The ratio of X-ray transmission intensity between a sample mounted on Kapton (background subtracted in SAXSGUI) was used along with the NIST X-ray absorption coefficient for $Nb_{14}W_3O_{44}$[118] to calculate the effective thickness of the powder monolayer as described in detail by Spalla *et al.*[106] This effective thickness was used to determine the absolute intensity scale later used for Porod surface area analysis of each powder.[119,120] The Porod region was determined as the q region with a near constant $I_{abs} \times q^4$ value and was used along with the scattering length density (ρ_{SLD}, NIST calculator[121]) to calculate the total quantity of the interface ($\sum$)

$$\sum = \frac{\lim_{q\to\infty} I_{abs} q^4}{2\pi(\Delta\rho_{SLD}{}^2)}$$

The total quantity of the interface and the bulk density of $Nb_{14}W_3O_{44}$ (ρ) were used to calculate the specific surface area, S:

$$S = \frac{\sum}{\rho}$$

X-ray photoelectron spectroscopy characterization

The surface electronic environments of the samples were investigated with the AXIS Ultra DLD XPS (Kratos Analytical) instrument. The XPS system is equipped with a Non-monochromatic Al Kα source (1486.8 eV) operated at 120 W. The X-rays were incident at an angle of 45° with respect to the sample surface. Analysis was performed at a pressure of ∼1 × 10^{-9} torr and high-resolution core level spectra were acquired in the constant analyzer energy mode using a pass energy of 40 eV and a 0.05 eV step Size. The XPS experiments were performed by using a low energy electron beam, directed at the sample, for charge neutralization. The curve fitting procedure was carried out using the Casa XPS software, and the peak approximation was carried out by Lorentzian asymmetric (LA) line shapes, with subtraction of Shirley-type backgrounds. Binding energies (BE) are in reference to the C1s peak at 285 eV (adventitious carbon from contamination) and given with an accuracy of ±0.2 eV.

DSC/TGA measurements

DSC measurements were done on a Hitachi 7020DSC using aluminum pans. The pans were loaded with approximately 2–3 mg of sample material before crimping a hermetic seal. All experiments were done with a laminar flow of N_2 with a variable heating rate between 2 and 20 °C min^{-1} with a temperature range of 20–450 °C. TGA experiments were done using a Hitachi STA7200 with flowing N_2. 10 mg of sample was loaded into a platinum sample holder and the measurement was heated between 50–700 °C with a heating rate of 10 °C min^{-1}. Both DSC and TGA data were analyzed in NEXTA software and plotted using custom MATLAB codes.

Raman spectroscopy

Raman spectroscopy was done using a Horiba LabRAM using a 532 nm laser. Data was analyzed using LabSpec6. Samples were finely ground and mounted on a glass microscope slide. All data was acquired using a 100× objective, hole size of 150, a diffraction grating of 600, and a laser power of 5% with 30 accumulations of 1 s pulses.

Author contributions

Sean Wechsler: conceptualization, methodology, data curation, formal analysis, writing, editing, Alexander Gregg: methodology, data curation, proofreading, Coby Collins: data curation, proofreading, Santosh Balijepalli: data curation, proofreading, Morgan Stefik: conceptualization, methodology, writing, editing, funding acquisition.

Data availability

The data supporting this article have been included as part of the ESI.† Custom Matlab scripts used for GPC analysis are available at: **https://stefikgroup.com//GPC/**. Raw data are available upon reasonable request.

Conflicts of interest

The authors declare no conflicts of interest.

Acknowledgements

SCW, AG, and MS acknowledge U.S. Department of Energy support (DE-SC0023377). CSC acknowledges support by the National Science Foundation under NSF Award No. DMR-1752615. This project made use of the South Carolina SAXS Collaborative. This project was supported by the University of South Carolina XPS facility, which receives financial support from the Office of the Vice President for Research.

References

1 B. Bera and N. Das, Synthesis of SBA-15 Graphene Oxide Composite Membrane Using Phenol–Formaldehyde Resin Pore Modifier for CO_2 Separation, *J. Am. Ceram. Soc.*, 2022, **105**(2), 913–928.

2 W. Gao, T. Zhou, B. Louis and Q. Wang, Hydrothermal Fabrication of High Specific Surface Area Mesoporous MgO with Excellent CO_2 Adsorption Potential at Intermediate Temperatures, *Catalysts*, 2017, **7**(4), 116.

3 Y. Li, W. Luo, N. Qin, J. Dong, J. Wei, W. Li, S. Feng, J. Chen, J. Xu, A. A. Elzatahry, M. H. Es-Saheb, Y. Deng and D. Zhao, Highly Ordered Mesoporous Tungsten Oxides with a Large Pore Size and Crystalline Framework for H_2S Sensing, *Angew. Chem., Int. Ed.*, 2014, **53**(34), 9035–9040.

4 X. Cui, H. Zhang, X. Dong, H. Chen, L. Zhang and J. Shi, Electrochemical Catalytic Activity for the Hydrogen Oxidation of Mesoporous WO_3 and WO_3/C Composites, *J. Mater. Chem.*, 2008, **18**, 3575–3580.

5 M. Hu, W. Yang, H. Tan, Y. Zhu, S. L. Suib, J. He, M. Hu, W. Yang, H. Tan, L. Jin, L. Zhang, P. Kerns and Y. Dang, Template-Free Synthesis of Mesoporous and Crystalline Transition Metal Oxide Nanoplates with Abundant Surface Defects, *Matter*, 2020, **2**(5), 1244–1259.

6 H. Wang, W. Guo, Z. Jiang, R. Yang, Z. Jiang and Y. Pan, New Insight into the Enhanced Activity of Ordered Mesoporous Nickel Oxide in Formaldehyde Catalytic Oxidation Reactions, *J. Catal.*, 2018, **361**, 370–383.

7 Z. Liu, Y. Du, R. Yu, M. Zheng, R. Hu, J. Wu, Y. Xia, Z. Zhuang and D. Wang, Tuning Mass Transport in Electrocatalysis Down to Sub-5 nm through Nanoscale Grade Separation, *Angew. Chem., Int. Ed.*, 2023, **62**(3), e202212653.

8 H. Kim, E. Lim, C. Jo, G. Yoon, J. Hwang, S. Jeong, J. Lee and K. Kang, Ordered-Mesoporous Nb_2O_5/Carbon Composite as a Sodium Insertion Material, *Nano Energy*, 2015, **16**, 62–70.

9 J. H. Pan, X. S. Zhao and W. I. Lee, Block Copolymer-Templated Synthesis of Highly Organized Mesoporous TiO_2-Based Films and Their Photoelectrochemical Applications, *Chem. Eng. J.*, 2011, **170**(2–3), 363–380.

10 C. Jo, J. Hwang, H. Song, A. H. Dao, Y. Kim, S. H. Lee, S. W. Hong, S. Yoon and J. Lee, Block-Copolymer-Assisted One-Pot Synthesis of Ordered Mesoporous WO_{3-x}/Carbon Nanocomposites as High-Rate-Performance Electrodes for Pseudocapacitors, *Adv. Funct. Mater.*, 2013, **23**(30), 3747–3754.

11 M. Dai, L. Song, J. T. Labelle and B. D. Vogt, Ordered Mesoporous Carbon Composite Films Containing Cobalt Oxide and Vanadia for Electrochemical Applications, *Chem. Mater.*, 2011, **23**(11), 2869–2878.

12 S. D. Han, S. Kim, D. Li, V. Petkov, H. D. Yoo, P. J. Phillips, H. Wang, J. J. Kim, K. L. More, B. Key, R. F. Klie, J. Cabana, V. R. Stamenkovic, T. T. Fister, N. M. Markovic, A. K. Burrell, S. Tepavcevic and J. T. Vaughey, Mechanism of Zn Insertion into Nanostructured δ-MnO_2: A Nonaqueous Rechargeable Zn Metal Battery, *Chem. Mater.*, 2017, **29**(11), 4874–4884.

13 L. Pan, H. Huang, T. Liu and M. Niederberger, Structurally Disordered Ta_2O_5 Aerogel for High-Rate and Highly Stable Li-Ion and Na-Ion Storage through Surface Redox Pseudocapacitance, *Electrochim. Acta*, 2019, **321**, 134645.

14 Y. Liu, K. Lan, A. A. Bagabas, P. Zhang, W. Gao, J. Wang, Z. Sun, J. Fan, A. A. Elzatahry and D. Zhao, Ordered Macro/Mesoporous TiO_2 Hollow Microspheres with Highly Crystalline Thin Shells for High-Efficiency Photoconversion, *Small*, 2015, **12**(7), 860–867.

15 J. Haetge, C. Suchomski and T. Brezesinski, Ordered Mesoporous β-$MgMoO_4$ Thin Films for Lithium-Ion Battery Applications, *Small*, 2013, **9**(15), 2541–2544.

16 H. Liu, X. Du, X. Xing and S. Zhang, Highly Ordered Mesoporous Cr_2O_3 Materials with Enhanced Performance for Gas Sensors and Lithium Ion Batteries, *Chem Commun.*, 2012, **48**, 865–867.

17 S. Lou, X. Cheng, L. Wang, J. Gao, Q. Li, Y. Ma, Y. Gao, P. Zuo, C. Du and G. Yin, High-Rate Capability of Three-Dimensionally Ordered Macroporous T-Nb_2O_5 through Li^+ Intercalation Pseudocapacitance, *J. Power Sources*, 2017, **361**, 80–86.

18 E. Umeshbabu, D. Velpula, G. Karkera, M. Satyanarayana, V. Pasala and P. Justin, Facile Synthesis of Ordered Mesoporous Orthorhombic Niobium Oxide (T-Nb_2O_5) for High-Rate Li-Ion Storage with Long Cycling Stability, *Batteries*, 2023, **9**(7), 357.

19 M. Einert, A. Waheed, S. Lauterbach, M. Mellin, M. Rohnke, L. Q. Wagner, J. Gallenberger, C. Tian, B. M. Smarsly, W. Jaegermann, F. Hess, H. Schlaad and J. P. Hofmann, Sol–Gel-Derived Ordered Mesoporous High Entropy Spinel Ferrites and Assessment of Their Photoelectrochemical and Electrocatalytic Water Splitting Performance, *Small*, 2023, **19**(14), 2205412.

20 A. K. Koopmann, J. Torres-Rodríguez, M. Salihovic, J. Schoiber, M. Musso, G. Fritz-Popovski, N. Huesing and M. S. Elsaesser, Tannin-Based Nanoscale Carbon Spherogels as Electrodes for Electrochemical Applications, *ACS Appl. Nano Mater.*, 2021, **4**(12), 14115–14125.

21 H. Yang and D. Zhao, Synthesis of Replica Mesostructures by the Nanocasting Strategy, *J. Mater. Chem.*, 2005, **15**, 1217–1231.

22 H. Tu, C. Weidenthaler, T. Grewe, E. L. Salabas, M. J. B. Romero and F. A. Schu, Crystal Structure Analysis and Magnetic Investigation on Highly Ordered Mesoporous Cr_2O_3, *Inorg. Chem.*, 2012, **51**(21), 11745–11752.
23 Y. Xia, Y. Zhao, Y. Li, F. Hu and L. Zhang, Vacuum-Assisted Hard-Templating Impregnation Fabrication of Three-Dimensional Ordered Mesoporous Samarium Oxide, *J. Porous Mater.*, 2016, **23**(6), 1591–1595.
24 S. Cabrera, J. El Haskouri, J. A. A. Beltran, D. Beltran, S. Mendioroz, M. D. Marcos and P. Amorós, Surfactant-Assisted Synthesis of Mesoporous Alumina Showing Continuously Adjustable Pore Sizes, *Adv. Mater.*, 1999, **11**(5), 379–381.
25 P. Yang, D. Zhao, D. I. Margolese, B. F. Chmelka and G. D. Stucky, Block Copolymer Templating Syntheses of Mesoporous Metal Oxides with Large Ordering Lengths and Semicrystalline Framework, *Chem. Mater.*, 1999, **11**(10), 2813–2826.
26 P. Yang, D. Zhao, D. I. Margolese, B. F. Chmelka and G. D. Stucky, Generalized Syntheses of Large-Pore Mesoporous Metal Oxides with Semicrystalline Frameworks, *Nature*, 1998, **396**(6707), 152–155.
27 J. Wu, X. Liu and S. H. Tolbert, High-Pressure Stability in Ordered Mesoporous Silicas: Rigidity and Elasticity through Nanometer Scale Arches, *J. Phys. Chem. B*, 2000, **104**(50), 11837–11841.
28 T. Brezesinski, B. Smarsly, K. I. Iimura, D. Grosso, C. Boissière, H. Amenitsch, M. Antonietti and C. Sanchez, Self-Assembly and Crystallization Behavior of Mesoporous, Crystalline HfO_2 Thin Films: A Model System for the Generation of Mesostructured Transition-Metal Oxides, *Small*, 2005, **1**(8–9), 889–898.
29 M. Jesus, J. Fornerod, A. Alvarez-fernandez, E. R. Williams, M. W. A. Skoda, B. Prieto-simon, N. H. Voelcker, M. Stefik, M. Coppens and S. Guldin, Enhanced Structural Control of Soft-Templated Mesoporous Inorganic Thin Films by Inert Processing Conditions, *ACS Appl. Mater. Interfaces*, 2022, **14**(50), 56143–56155.
30 J. Zhang, Y. Deng, D. Gu, S. Wang, L. She, R. Che, Z. S. Wang, B. Tu, S. Xie and D. Zhao, Ligand-Assisted Assembly Approach to Synthesize Large-Pore Ordered Mesoporous Titania with Thermally Stable and Crystalline Framework, *Adv. Energy Mater.*, 2011, **1**(2), 241–248.
31 T. Brezesinski, Large-Pore Mesoporous $Ho_3Fe_5O_{12}$ Thin Films with a Strong Room- Temperature Perpendicular Magnetic Anisotropy by Sol−Gel Processing, *Chem. Mater.*, 2014, **26**(7), 2337–2343.
32 C. Reitz, J. Haetge, C. Suchomski and T. Brezesinski, Facile and General Synthesis of Thermally Stable Ordered Mesoporous Rare-Earth Oxide Ceramic Thin Films with Uniform Mid-Size to Large-Size Pores and Strong Crystalline Texture, *Chem. Mater.*, 2013, **25**(22), 4633–4642.
33 D. M. Antonelli and J. Y. Ying, Synthesis of Hexagonally Packed Mesoporous TiO_2 by a Modified Sol–Gel Method, *Angew. Chem., Int. Ed. Engl.*, 1995, **34**(18), 2014–2017.
34 D. M. Antonelli, Synthesis of Phosphorus-Free Mesoporous Titania via Templating with Amine Surfactants, *Microporous Mesoporous Mater.*, 1999, **30**(2–3), 315–319.
35 P. Cop, E. Celik, K. Hess, Y. Moryson, P. Klement, M. T. Elm and B. M. Smarsly, Atomic Layer Deposition of Nanometer-Sized CeO_2 Layers in Ordered Mesoporous ZrO_2 Films and Their Impact on the Ionic/Electronic Conductivity, *ACS Appl. Nano Mater.*, 2020, **3**(11), 10757–10766.
36 T. Brezesinski, D. F. Rohlfing, S. Sallard, M. Antonietti and B. M. Smarsly, Highly Crystalline WO_3 Thin Films with Ordered 3D Mesoporosity and Improved Electrochromic Performance, *Small*, 2006, **2**(10), 1203–1211.
37 Q. Yuan, L. Li, S. Lu, H. Duan, Z. Li, Y. Zhu and C. Yan, Facile Synthesis of Zr-Based Functional Materials with Highly Ordered Mesoporous Structures, *J. Phys. Chem. C*, 2009, **113**(10), 4117–4124.
38 S. Gurung, F. Gucci, G. Cairns, I. Chianella and G. J. T. Leighton, Hollow Silica Nano and Micro Spheres with Polystyrene Templating: A Mini-Review, *Materials*, 2022, **15**, 8578.
39 U. Ciesla, D. Demuth, R. Leon, P. Petroff, G. Stucky, K. Unger and F. Schüth, Surfactant Controlled Preparation of Mesostructured Transition-Metal Oxide Compounds, *J. Chem. Soc., Chem. Commun.*, 1994, **11**, 1387–1388.
40 E. R. Williams, C. X. Ruff and M. Stefik, Unimer Suppression Enables Supersaturated Homopolymer Swollen Micelles with Long-Term Stability after Glassy Entrapment, *Soft Matter*, 2024, **20**(10), 2288–2300.
41 K. Peters, H. N. Lokupitiya, D. Sarauli, M. Labs, M. Pribil, J. Rathouský, A. Kuhn, D. Leister, M. Stefik and D. Fattakhova-Rohlfing, Nanostructured Antimony-Doped Tin Oxide Layers with Tunable Pore Architectures as Versatile Transparent Current Collectors for Biophotovoltaics, *Adv. Funct. Mater.*, 2016, **26**(37), 6682–6692.
42 W. Van Den Bergh, E. R. Williams, N. A. Vest, P. H. Chiang and M. Stefik, Mesoporous TiO_2 Microparticles with Tailored Surfaces, Pores, Walls, and Particle Dimensions Using Persistent Micelle Templates, *Langmuir*, 2021, **37**(44), 12874–12886.
43 T. Larison and M. Stefik, Persistent Micelle Corona Chemistry Enables Constant Micelle Core Size with Independent Control of Functionality and Polyelectrolyte Response, *Langmuir*, 2021, **37**(32), 9817–9825.
44 E. R. Williams, P. L. McMahon, J. Reynolds III, J. L. Snider, V. Stavila, M. D. Allendorf and M. Stefik, Tailored Porous Carbons Enabled by Persistent Micelles with Glassy Cores, *Mater. Adv.*, 2021, **2**, 5381–5395.
45 K. A. Lantz, N. B. Clamp, W. van den Bergh, A. Sarkar and M. Stefik, Full Gamut Wall Tunability from Persistent Micelle Templates via *Ex Situ* Hydrolysis, *Small*, 2019, **15**(18), 1–10.
46 H. N. Lokupitiya, A. Jones, B. Reid, S. Guldin and M. Stefik, Ordered Mesoporous to Macroporous Oxides with Tunable Isomorphic Architectures: Solution Criteria for Persistent Micelle Templates, *Chem. Mater.*, 2016, **28**(6), 1653–1667.
47 M. Stefik, J. Song, H. Sai, S. Guldin, P. Boldrighini, M. C. Orilall, U. Steiner, S. M. Gruner and U. Wiesner, Ordered Mesoporous Titania from Highly Amphiphilic Block Copolymers: Tuned Solution Conditions Enable

Highly Ordered Morphologies and Ultra-Large Mesopores, *J. Mater. Chem. A*, 2015, **3**(21), 11478–11492.

48 E. L. Crepaldi, G. J. de, A. A. Soler-Illia, D. Grosso, F. Cagnol, F. Ribot and C. Sanchez, Controlled Formation of Highly Organized Mesoporous Titania Thin Films: From Mesostructured Hybrids to Mesoporous Nanoanatase TiO_2, *J. Am. Chem. Soc.*, 2003, **125**(32), 9770–9786.

49 B. L. Kirsch, E. K. Richman, A. E. Riley and S. H. Tolbert, *In Situ* X-Ray Diffraction Study of the Crystallization Kinetics of Mesoporous Titania Films, *J. Phys. Chem. B*, 2004, **108**(34), 12698–12706.

50 D. Grosso, G. J. de, A. A. Soler-Illia, E. L. Crepaldi, F. Cagnol, C. Sinturel, A. Bourgeois, A. Brunet-Bruneau, H. Amenitsch, P. A. Albouy and C. Sanchez, Highly Porous TiO_2 Anatase Optical Thin Films with Cubic Mesostructure Stabilized at 700 °C, *Chem. Mater.*, 2003, **15**(24), 4562–4570.

51 B. Smarsly, D. Grosso, T. Brezesinski, N. Pinna, C. Boissière, M. Antonietti and C. Sanchez, Highly Crystalline Cubic Mesoporous TiO_2 with 10-Nm Pore Diameter Made with a New Block Copolymer Template, *Chem. Mater.*, 2004, **16**(15), 2948–2952.

52 H. Liang, L. Liu, N. Wang, W. Zhang, C. Hung, X. Zhang, Z. Zhang, L. Duan, D. Chao, F. Wang, Y. Xia, W. Li and D. Zhao, Unusual Mesoporous Titanium Niobium Oxides Realizing Sodium-Ion Batteries Operated at −40 °C, *Adv. Mater.*, 2022, **34**(28), 2202873.

53 T. Katou, B. Lee, D. Lu, J. N. Kondo, M. Hara and K. Domen, Crystallization of an Ordered Mesoporous Nb–Ta Oxide, *Agnew. Chem., Int. Ed.*, 2003, **42**, 2382–2385.

54 K. S. A. Halim, A. A. El-Geassy, M. Ramadan, M. I. Nasr, A. Hussein, N. Fathy and A. S. Alghamdi, Reduction Behavior and Characteristics of Metal Oxides in the Nanoscale, *Metals*, 2022, **12**(12), 2182.

55 A. Kadkhodayan and A. Brenner, Temperature-Programmed Reduction and Oxidation of Metals Supported on γ-Alumina, *J. Catal.*, 1989, **117**(2), 311–321.

56 S. Wu, C. Zhou, E. Doroodchi, R. Nellore and B. A. Moghtaderi, A Review on High-Temperature Thermochemical Energy Storage Based on Metal Oxides Redox Cycle, *Energy Convers. Manage.*, 2018, **168**, 421–453.

57 A. A. Voskanyan, K. Jayanthi and A. Navrotsky, Vacancy Control in $TiNb_2O_7$: Implications for Energy Applications, *Chem. Mater.*, 2022, **34**(23), 10311–10319.

58 S. Deng, Y. Zhang, D. Xie, L. Yang, G. Wang, X. S. Zheng, J. Zhu, X. Wang, Y. Yu, G. Pan, X. Xia and J. Tu, Oxygen Vacancy Modulated $Ti_2Nb_{10}O_{29-x}$ Embedded onto Porous Bacterial Cellulose Carbon for Highly Efficient Lithium Ion Storage, *Nano Energy*, 2019, **58**, 355–364.

59 Y. Zhang, M. Zhang, Y. Liu, H. Zhu, L. Wang, Y. Liu, M. Xue, B. Li and X. Tao, Oxygen Vacancy Regulated $TiNb_2O_7$ Compound with Enhanced Electrochemical Performance Used as Anode Material in Li-Ion Batteries, *Electrochim. Acta*, 2020, **330**, 135299.

60 J. H. Lin, Y. T. Yan, J. L. Qi and C. Y. Zha, Atomic Tailoring-Induced Deficiency in Tungsten Oxides for High-Performance Energy-Related Devices, *Tungsten*, 2024, **6**(2), 269–277.

61 M. Reynaud, J. Serrano-Sevillano and M. Casas-Cabanas, Imperfect Battery Materials: A Closer Look at the Role of Defects in Electrochemical Performance, *Chem. Mater.*, 2023, **35**(9), 3345–3363.

62 S. Sun, L. Qin, Y. Sun and C. Guo, Plasma-Induced Defect Engineering in $TiNb_2O_7$ for Boosting Lithium-Ion Diffusion, *Energy Fuels*, 2024, **38**(3), 2463–2471.

63 X. Chen, L. Liu, P. Y. Yu and S. S. Mao, Increasing Solar Absorption for Photocatalysis with Black Hydrogenated Titanium Dioxide Nanocrystals, *Science*, 2011, **331**(6018), 746–750.

64 Y. Shang, S. Lu, W. Zheng, R. Wang, Z. Liang, Y. Huang, J. Mei, Y. Yang, W. Zeng and H. Zhan, Facile Synthesis of Carbon and Oxygen Vacancy Co-Modified $TiNb_6O_{17}$ as an Anode Material for Lithium-Ion Batteries, *RSC Adv.*, 2022, **12**(21), 13127–13134.

65 J. G. Allpress, Mixed Oxides of Titanium and Niobium: Defects in Quenched Samples, *J. Solid State Chem.*, 1970, **2**(1), 78–93.

66 M. A. Al Muhit, S. C. Wechsler, Z. J. L. Bare, C. J. Sturgill, N. Keerthisinghe, M. A. Grasser, G. Morrison, C. Sutton, M. Stefik and H. C. zur Loye, Comparison of Lithium Diffusion in Isostructural $Ta_{12}MoO_{33}$ and $Nb_{12}MoO_{33}$: Experimental and Computational Insights from Single Crystals, *Chem. Mater.*, 2024, **36**(21), 10626–10639.

67 A. R. Patterson, R. Elizalde-Segovia, K. E. Wyckoff, A. Zohar, P. P. Ding, W. M. Turner, K. R. Poeppelmeier, S. R. Narayan, R. J. Clément, R. Seshadri and K. J. Griffith, Rapid and Reversible Lithium Insertion in the Wadsley-Roth-Derived Phase $NaNb_{13}O_{33}$, *Chem. Mater.*, 2023, **35**(16), 6364–6373.

68 Y. Zhou, E. Le Calvez, S. W. Baek, M. Frajnkovič, C. Douard, E. Gautron, O. Crosnier, T. Brousse and L. Pilon, Effect of Particle Size on Thermodynamics and Lithium Ion Transport in Electrodes Made of $Ti_2Nb_2O_9$ Microparticles or Nanoparticles, *Energy Storage Mater.*, 2022, **52**, 371–385.

69 C. Guo, Z. Liu, K. Han, L. Zhang, X. Ding, X. Wang and L. Mai, Nano-Sized Niobium Tungsten Oxide Anode for Advanced Fast-Charge Lithium-Ion Batteries, *Small*, 2022, **18**(12), 1–9.

70 B. D. Sten Andersson and D. A. Wadsley, Crystallographic Shear and Diffusion Paths in Certain Higher Oxides of Niobium, Tungsten, Molybdenum and Titanium, *Nature*, 1966, **211**, 581–583.

71 X. H. Ma, X. Cao, Y. Y. Ye, F. Qiao, M. F. Qian, Y. Y. Wei, Y. D. Wu, Z. F. Zi and J. M. Dai, Study on Low-Temperature Performances of $Nb_{16}W_5O_{55}$ Anode for Lithium-Ion Batteries, *Solid State Ionics*, 2020, **353**, 115376.

72 K. J. Griffith and C. P. Grey, Superionic Lithium Intercalation through 2 × 2 Nm Columns in the Crystallographic Shear Phase $Nb_{18}W_8O_{69}$, *Chem. Mater.*, 2020, **32**(9), 3860–3868.

73 H. Zou, Effect of Synthetic Conditions on the Structure and Properties of $Nb_{14}W_3O_{44}$ Anode for Lithium-Ion Batteries, *Chem. Eng. Technol.*, 2023, **46**(10), 2054–2062.

74 K. Ariyoshi and N. Ohji, Synthesis and Characterization of W–Nb Oxides (WO_3–Nb_2O_5) for Large-Volumetric-Capacity Negative Electrodes, *ACS Appl. Energy Mater.*, 2023, **6**(14), 7497–7508.
75 X. Huang, W. Zhou, X. Chen, C. Jiang and Z. Zou, High Performance Li-Ion Hybrid Capacitors with Micro-Sized $Nb_{14}W_3O_{44}$ as Anode, *Electrochim. Acta*, 2021, **368**, 137613.
76 H. H. Otto, Fibonacci Stoichiometry and Superb Performance of $Nb_{16}W_5O_{55}$ and Related Super-Battery Materials, *J. At. Mol. Phys.*, 2022, **10**(6), 1936–1950.
77 L. D. Salzer, B. Diamond, K. Nieto, R. C. Evans, A. L. Prieto and J. B. Sambur, Structure−Property Relationships in High-Rate Anode Materials Based on Niobium Tungsten Oxide Shear Structures, *ACS Appl. Energy Mater.*, 2023, **6**(3), 1685–1691.
78 K. J. Griffith, K. M. Wiaderek, G. Cibin, L. E. Marbella and C. P. Grey, Niobium Tungsten Oxides for High-Rate Lithium-Ion Energy Storage, *Nature*, 2018, **559**(7715), 556–563.
79 C. P. Koçer, K. J. Griffith, C. P. Grey and A. J. Morris, Lithium Diffusion in Niobium Tungsten Oxide Shear Structures, *Chem. Mater.*, 2020, **32**(9), 3980–3989.
80 W. van den Bergh and M. Stefik, Understanding Rapid Intercalation Materials One Parameter at a Time, *Adv. Funct. Mater.*, 2022, **32**(31), 2204126.
81 W. van den Bergh, H. N. Lokupitiya, N. A. Vest, B. Reid, S. Guldin and M. Stefik, Nanostructure Dependence of T-Nb_2O_5 Intercalation Pseudocapacitance Probed Using Tunable Isomorphic Architectures, *Adv. Funct. Mater.*, 2021, **31**(1), 2007826.
82 F. Vaudry, S. Khodabandeh and M. E. Davis, Synthesis of Pure Alumina Mesoporous Materials, *Chem. Mater.*, 1996, **8**(7), 1451–1464.
83 B. Reid, A. Alvarez-Fernandez, B. Schmidt-Hansberg and S. Guldin, Tuning Pore Dimensions of Mesoporous Inorganic Films by Homopolymer Swelling, *Langmuir*, 2019, **35**(43), 14074–14082.
84 M. Kamperman, C. B. W. Garcia, P. Du, H. Ow and U. Wiesner, Ordered Mesoporous Ceramics Stable up to 1500 °C from Diblock Copolymer Mesophases, *J. Am. Chem. Soc.*, 2004, **126**(45), 14708–14709.
85 C. Suchomski, C. Reitz, C. T. Sousa, J. P. Araujo and T. Brezesinski, Room Temperature Magnetic Rare-Earth Iron Garnet Thin Films with Ordered Mesoporous Structure, *Chem. Mater.*, 2013, **25**(12), 2527–2537.
86 J. Haetge, C. Reitz, C. Suchomski and T. Brezesinski, Toward Ordered Mesoporous Rare-Earth Sesquioxide Thin Films via Polymer Templating: High Temperature Stable C-Type Er_2O_3 with Finely-Tunable Crystallite Sizes, *RSC Adv.*, 2012, **2**(18), 7053–7056.
87 J. Ba, J. Polleux, M. Antonietti and M. Niederberger, Non-Aqueous Synthesis of Tin Oxide Nanocrystals and Their Assembly into Ordered Porous Mesostructures, *Adv. Mater.*, 2005, **17**(20), 2509–2512.
88 J. Fan, S. W. Boettcher and G. D. Stucky, Nanoparticle Assembly of Ordered Multicomponent Mesostructured Metal Oxides via a Versatile Sol–Gel Process, *Chem. Mater.*, 2006, **18**(26), 6391–6396.
89 D. Li, H. Zhou and I. Honma, Design and Synthesis of Self-Ordered Mesoporous Nanocomposite through Controlled *in Situ* Crystallization, *Nat. Mater.*, 2004, **3**(1), 65–71.
90 A. Zelcer and G. J. A. A. Soler-illa, One-step Preparation of UV Transparent Highly Ordered Mesoporous Zirconia Thin Films, *J. Mater. Chem. C*, 2013, **1**, 1359–1367.
91 R. Liu, Y. Ren, Y. Shi, F. Zhang, L. Zhang, B. Tu and D. Zhao, Controlled Synthesis of Ordered Mesoporous C-TiO_2 Nanocomposites with Crystalline Titania Frameworks from Organic–Inorganic-Amphiphilic Coassembly, *Chem. Mater.*, 2008, **20**(3), 1140–1145.
92 J. Tang, Y. Wu, E. W. McFarland and G. D. Stucky, Synthesis and Photocatalytic Properties of Highly Crystalline and Ordered Mesoporous TiO_2 Thin Films, *Chem. Commun.*, 2004, (14), 1670–1671.
93 J. Lee, M. Christopher Orilall, S. C. Warren, M. Kamperman, F. J. Disalvo and U. Wiesner, Direct Access to Thermally Stable and Highly Crystalline Mesoporous Transition-Metal Oxides with Uniform Pores, *Nat. Mater.*, 2008, **7**(3), 222–228.
94 B. Tian, X. Liu, B. Tu, C. Yu, J. Fan, L. Wang, S. Xie, G. D. Stucky and D. Zhao, Self-Adjusted Synthesis of Ordered Stable Mesoporous Minerals by Acid–Base Pairs, *Nat. Mater.*, 2003, **2**(3), 159–163.
95 O. J. Klejnot, Chloride Alkoxides of Pentavalent Tungsten, *Inorg. Chem.*, 1965, **4**(11), 1668–1670.
96 L. Michiels and A. Fischer, Studie Über Ein Derivat Des Filnfwertigen Wolframs, *Z. Anorg. Chem.*, 1912, **81**(1), 102–115.
97 A. Sarkar and M. Stefik, How to Make Persistent Micelle Templates in 24 Hours and Know It Using X-Ray Scattering, *J. Mater. Chem. A*, 2017, **5**(23), 11840–11853.
98 K. A. Lantz, N. B. Clamp, W. van den Bergh, A. Sarkar and M. Stefik, Full Gamut Wall Tunability from Persistent Micelle Templates via *Ex Situ* Hydrolysis, *Small*, 2019, **15**(18), 1900393.
99 T. Horikawa, K. Ogawa, K. Mizuno, J. Hayashi and K. Muroyama, Preparation and Characterization of the Carbonized Material of Phenol–Formaldehyde Resin with Addition of Various Organic Substances, *Carbon*, 2003, **41**(3), 465–472.
100 Y. Meng, D. Gu, F. Zhang, Y. Shi, H. Yang, Z. Li, C. Yu, B. Tu and D. Zhao, Ordered Mesoporous Polymers and Homologous Carbon Frameworks: Amphiphilic Surfactant Templating and Direct Transformation, *Angew. Chem., Int. Ed.*, 2005, **44**, 7053–7059.
101 G. He and B. Riedl, Curing Kinetics of Phenol Formaldehyde Resin and Wood-Resin Interactions in the Presence of Wood Substrates, *Wood Sci. Technol.*, 2004, **38**(1), 69–81.
102 A. Pizzi, B. Mtsweni and W. Parsons, Wood-induced Catalytic Activation of PF Adhesives Autopolymerization vs. PF/Wood Covalent Bonding, *J. Appl. Polym. Sci.*, 1994, **52**(13), 1847–1856.
103 Y. K. Lee, D. J. Kim, H. J. Kim, T. S. Hwang, M. Rafailovich and J. Sokolov, Activation Energy and Curing Behavior of Resol and Novolac-Type Phenolic Resins by Differential Scanning Calorimetry and Thermogravimetric Analysis, *J. Appl. Polym. Sci.*, 2003, **89**(10), 2589–2596.

104 C. P. Gabrielli and F. A. Kamke, Phenol–Formaldehyde Impregnation of Densified Wood for Improved Dimensional Stability, *Wood Sci. Technol.*, 2010, **44**(1), 95–104.
105 T. Furuno, Y. Imamura and H. Kajita, The Modification of Wood by Treatment with Low Molecular Weight Phenol–Formaldehyde Resin: A Properties Enhancement with Neutralized Phenolic-Resin and Resin Penetration into Wood Cell Walls, *Wood Sci. Technol.*, 2004, **37**(5), 349–361.
106 O. Spalla, S. Lyonnard and F. Testard, Analysis of the Small-Angle Intensity Scattered by a Porous and Granular Medium, *J. Appl. Crystallogr.*, 2003, **36**(2), 338–347.
107 W. A. Goddard, On the Wrong Assingment of the XPS O 1s Signal at 531–532 eV Attributed to Oxygen Vacancies in Photo- and Electro-catalysts for Water Splitting and Other Materials, *Surf. Sci.*, 2021, **712**, 121894.
108 F. V. E. Hensling, C. Xu, F. Gunkel and R. Dittmann, Unraveling the Enhanced Oxygen Vacancy Formation in Complex Oxides during Annealing and Growth, *Sci. Rep.*, 2017, **7**, 39953.
109 G. Zhuang, Y. Chen, Z. Zhuang, Y. Yu and J. Yu, Oxygen Vacancies in Metal Oxides: Recent Progress towards Advanced Catalyst Design, *Sci. China Mater.*, 2020, **63**(11), 2089–2118.
110 Z. Li, L. Deng, I. A. Kinloch and R. J. Young, Raman Spectroscopy of Carbon Materials and Their Composites: Graphene, Nanotubes and Fibres, *Prog. Mater. Sci.*, 2023, **135**, 101089.
111 Y. C. Uz and M. Tanoğlu, Determination of Activation Energy for Carbon/Epoxy Prepregs Containing Carbon Nanotubes by Differential Scanning Calorimetry, *High Perform. Polym.*, 2023, **35**(2), 166–180.
112 J. C. M. Torfs, L. Deij, A. J. Dorrepaal and J. C. Heijens, Determination of Arrhenius Kinetic Constants by Differential Scanning Calorimetry, *Anal. Chem.*, 1984, **56**(14), 2863–2867.
113 T. Ozawa, Kinetic Analysis of Derivative Curves in Thermal Analysis, *J. Therm. Anal.*, 1970, **2**(3), 301–324.
114 R. T. Yang and M. Steinberg, Reaction Kinetic and Differential Thermal Analysis, *J. Phys. Chem.*, 1976, **80**(9), 965–968.
115 G. P. Shulman and W. Lochte, Thermal Degradation of Polymers. IV. Poly-2,2′-(m-Phenylene)-5,5′-Bibenzimidazole, *J. Macromol. Sci., Part A: Pure Appl. Chem.*, 1967, **1**(3), 413–428.
116 H. E. Kissinger, Reaction Kinetics in Differential Thermal Analysis, *Anal. Chem.*, 1957, **29**(11), 1702–1706.
117 R. Whitfield, A. Anastasaki, V. Nikolaou, G. R. Jones, N. G. Engelis, E. H. Discekici, C. Fleischmann, J. Willenbacher, C. J. Hawker and D. M. Haddleton, Universal Conditions for the Controlled Polymerization of Acrylates, Methacrylates, and Styrene *via* Cu(0)-RDRP, *J. Am. Chem. Soc.*, 2017, **139**(2), 1003–1010.
118 NIST X-ray Form Factor, Attenuation, and Scattering Tables, Available at: **https://physics.nist.gov/PhysRefData/FFast/html/form.html**, Acessed January 10th, 2025.
119 C. Schlumberger, C. Scherdel, M. Kriesten, P. Leicht, A. Keilbach, H. Ehmann, P. Kotnik, G. Reichenauer and M. Thommes, Reliable Surface Area Determination of Powders and Meso/Macroporous Materials: Small-Angle X-Ray Scattering and Gas Physisorption, *Microporous Mesoporous Mater.*, 2022, **329**, 111554.
120 G. Beaucage, T. A. Ulibarri, E. P. Black and D. W. Schaefer, Multiple Size Scale Structures in Silica—Siloxane Composites Studied by Small-Angle Scattering, *Hybrid Organic–Inorganic Composites*, 1995, ch. 9, pp. 97–111.
121 NIST Center for Neutron Research Scattering Length Density Calculator, Available at: **https://www.ncnr.nist.gov/resources/activation/**, Acessed January 10th, 2025.

